

Flows and Non-thermal Velocities in Solar Active Regions Observed with the Extreme-ultraviolet Imaging Spectrometer on *Hinode*: A Tracer of Active Region Sources of Heliospheric Magnetic Fields?

G. A. Doschek, H. P. Warren, J. T. Mariska

Space Science Division, Naval Research Laboratory, Washington, DC 20375, USA

`george.doschek@nrl.navy.mil`

K. Muglach

ARTEP, Inc., Ellicott City, MD

J. L. Culhane

*Mullard Space Science Laboratory, University College London, Holmbury St. Mary,
Dorking, Surrey, RH5 6NT, UK*

H. Hara, T. Watanabe

National Astronomical Observatory, Mitaka, Tokyo 181-8588

ABSTRACT

From Doppler velocity maps of active regions constructed from spectra obtained by the Extreme-ultraviolet Imaging Spectrometer (EIS) on the *Hinode* spacecraft we observe large areas of outflow ($20\text{--}50\text{ km s}^{-1}$) that can persist for at least a day. These outflows occur in areas of active regions that are faint in coronal spectral lines formed at typical quiet Sun and active region temperatures. The outflows are positively correlated with non-thermal velocities in coronal plasmas. The bulk mass motions and non-thermal velocities are derived from spectral line centroids and line widths, mostly from a strong line of Fe XII at 195.12 Å. The electron temperature of the outflow regions estimated from an Fe XIII to Fe XII line intensity ratio is about $1.2 - 1.4 \times 10^6$ K. The electron density of the outflow regions derived from a density sensitive intensity ratio of Fe XII lines is rather low for an active region. Most regions average around $7 \times 10^8\text{ cm}^{-3}$, but there are variations on pixel spatial scales of about a factor of 4. We discuss results in detail for two active regions observed by EIS. Images of active regions

in line intensity, line width, and line centroid are obtained by rastering the regions. We also discuss data from the active regions obtained from other orbiting spacecraft that support the conclusions obtained from analysis of the EIS spectra. The locations of the flows in the active regions with respect to the longitudinal photospheric magnetic fields suggest that these regions might be tracers of long loops and/or open magnetic fields that extend into the heliosphere, and thus the flows could possibly contribute significantly to the solar wind.

Subject headings: Sun: solar atmosphere, extreme-ultraviolet

1. INTRODUCTION

The launch of the Extreme-ultraviolet Imaging Spectrometer (EIS) on the *Hinode* spacecraft on September 23, 2006 has given us the opportunity to investigate the dynamics of coronal plasma, i.e, bulk plasma flows and non-thermal motions, in more detail and with higher spatial resolution than previously possible. In addition, the dynamics can be associated with plasma diagnostic measurements of electron temperature and density. EIS can therefore help address fundamental unsolved problems in active region physics, such as heating in active region loops (e.g., Klimchuk 2006; Warren & Winebarger 2007), and the associations of active regions with the solar wind and heliospheric magnetic flux (e.g., Liewer, Neugebauer, & Zurbuchen 2004; Schrijver & DeRosa 2003).

Plasma motions might be particularly useful as tracers of either active region heating or sources of solar wind and heliospheric flux. For example, motions that are highly transient, spatially well-localized and comprised of both upflows and downflows, might signify active region loop heating and wave activity. In contrast, motions which are uni-directional (either upflows or downflows), lasting over several days, and that cover an extensive spatial region might be expected to be associated with primarily long loops or open field regions, and are possible indicators of sufficiently open magnetic flux to extend into the heliosphere and thus the flows could contribute to the solar wind. The association of flows with closed or open field can be facilitated by the creation of flow maps of active regions constructed by rastering the EIS spectrometer slit over an active region, and then correlating the maps with the underlying photospheric magnetic field.

Obtaining rasters of active regions and the creation of Doppler velocity flow maps was an early science goal of the EIS data analysis program. Doschek et al. (2007) (and more recently Harra et al. 2008) showed that in active regions there are extensive areas of low intensity that are characterized by net bulk plasma outflows and enhanced non-thermal motions. The

appearance of these outflow regions in areas of very low intensity is striking when compared with maps of spectral line intensity, also constructed from the EIS rasters. In this paper we expand the results of Doschek et al. (2007) and discuss in detail EIS rasters of Doppler shifts and non-thermal motions for two active regions. We estimate electron temperatures and densities of the outflowing regions, discuss data from other *Hinode* instruments and other satellites, and speculate on the types of magnetic structures that contain the flows and turbulent motions. We also estimate the mass flux of the flows into the corona. We will show that the locations of the flows in the active regions and the underlying morphology of the photospheric longitudinal magnetic flux suggest a link with heliospheric open fields that originate in active regions. The flows seem more associated with the solar wind and heliospheric magnetic fields than with heating of active region loops.

Experimentally, flows are determined from measurements of a spectral line centroid, coupled with information on the rest wavelength of the line. There are numerous observations of Doppler shifts in the literature, the most recent being obtained from the Solar Ultraviolet Measurements of Emitted Radiation (SUMER) spectrometer on the *Solar and Heliospheric Observatory* (e.g., Teriaca et al. 1999a; Warren, Mariska, & Wilhelm 1997). Mass motions can be related to heating in coronal flux tubes and the acceleration of the solar wind (e.g., Hassler et al. 1999; Tu et al. 2005; McIntosh et al. 2006). The solar wind work has centered mostly on Doppler shift measurements in coronal holes. There are also numerous coronal flux tube dynamical numerical simulation models in the literature (e.g., Hansteen 1993; Warren & Winebarger 2007; and Patsourakos & Klimchuk 2006). These models attempt to explain observed density and temperature measurements in coronal loops and relate the results to coronal heating mechanisms.

The origin of excess optically thin spectral line widths beyond their thermal Doppler widths is unclear. Since a rocket flight by Boland et al. (1975) it has been known that spectral lines from ions present in the solar transition region and corona have wider profiles than expected from pure thermal Doppler broadening alone, based on the ionization equilibrium temperatures at which they are formed. The profiles of the majority of the lines are Gaussian or close to Gaussian, and the excess broadening does not appear to be a strong function of position on the solar disk. The bulk of our current knowledge of these motions in non-flaring plasma has been obtained from the S082-B slit spectrograph on *Skylab* (e.g., Mariska 1992), the High Resolution Telescope Spectrograph (HRTS) rocket stigmatic spectrograph (e.g., Bartoe 1982), and SUMER (e.g., Chae, Schühle, & Lemaire 1998a).

The excess spectral line broadening is usually expressed as a non-thermal random mass motion component of unknown origin. It has been cited as an expected signature of waves in the corona (e.g., Mariska, Feldman, & Doschek 1978) and magnetic reconnection (e.g.,

Parker 1988). It could also be due to different multiple plasma flow speeds in structures smaller than the spatial resolution of the spectrometer because the convolved Gaussian-like line profile would be wider than the widths of the individual Gaussians composing the overall profile. Most recently, McIntosh et al. (2008) argue from *Hinode* high spatial resolution Solar Optical Telescope (SOT) observations that Alfvénic waves observed in small-scale spicular-type structures are responsible for the excess broadening.

Although there are numerous published observations of Doppler shifts and non-thermal motions, there is little information, particularly for the corona, on the detailed relationship of the motions to actual structures, e.g., coronal loops. There is far less information on the relationship of these dynamical parameters to other physical parameters such as electron temperature and density. The apparent close relationship between large line widths and bulk plasma flows seen in the EIS spectra is one of the most interesting aspects of the new observations.

In Section 2 we present pertinent details of the EIS on *Hinode*. In Section 3 we discuss the observations and data reduction. Results are given in Section 4 and the implications of the results are discussed in section 5.

2. THE EIS ON HINODE

The EIS is described in detail by Culhane et al. (2007) and Korendyke et al. (2006). The instrument consists of a multi-layer telescope and spectrometer. The telescope mirror and spectrometer grating are divided into two halves, each of which is coated with different Mo/Si multi-layers. This results in two observed extreme-ultraviolet narrow wavebands: 170-210 Å and 250-290 Å. Light from the telescope is focused onto the entrance aperture of the spectrometer. The grating then diffracts and focuses the light onto two CCD detectors.

The telescope mirror is articulated and different regions of the Sun can be focused onto the spectrometer aperture by fine mirror motions. The entrance aperture of the spectrometer can be one of four options: a 1" slit, a 2" slit, a 40" slot, or a 266" slot. The slits/slots are oriented in the solar north/south direction. Their heights can be variable, with a maximum height for most observations of 512".

There are several modes in which EIS can be operated. Images of solar regions can be constructed by rastering a slit or slot west to east across a given solar area with a set exposure time at each step. At each raster position it is possible to read-out the entire CCD and obtain a complete spectrum for each wavelength band. It is also possible to select a small set of lines, falling in narrower spectral windows, the choices of which depend on the

objectives of the observation.

The spatial resolution of EIS along the slit is approximately 2" (1" per pixel) and the spectral dispersion is quite high, 0.0223 Å per pixel. The instrumental full width at half maximum measured in the laboratory prior to launch is 1.956 pixels. However, we adopt an in-orbit instrumental width of 2.5 pixels, or 0.056 Å. This width was obtained by comparing the width of the EIS Fe XII 193.51 Å line observed above the limb with Fe XII forbidden line observations made from the *Skylab* S082-B spectrograph (Cheng, Doschek, & Feldman 1979) and SUMER (Doschek & Feldman 2000). The in-orbit instrument width is still being investigated, and may undergo small revisions in the future.

3. OBSERVATIONS AND DATA REDUCTION

Data from two active regions were examined for this work. These regions are listed in Table 1, along with the start times of the EIS observations, the solar locations, and the EIS exposure times. The locations are given in arcseconds relative to Sun center. Positive locations are west/north; negative ones are east/south. The observations consist of rasters using the 1" slit stepped from west to east in 1" increments for a total of 255 pointings. The slit height is 256 pixels. Each spectrum at each location in the raster contains 20 spectral lines, in 16 pixel wide spectral windows. The locations in Table 1 refer to the centers of the rasters. Data from other active regions have been qualitatively examined and support the general conclusions from the two regions discussed herein.

Most of the line width and position results discussed in this paper were obtained from the 195.12 Å Fe XII line. This is the most intense line in the EIS spectrum in part because its wavelength is near the maximum of the multi-layer efficiency. It is therefore ideal for line profile measurements because good count rates are available for statistically meaningful results. In addition, the ratio of Fe XII lines (186.89+186.85)/195.12) is used to obtain electron densities, and the ratio of an Fe XIII 202.04 Å line to the Fe XII 195.12 Å line is used to detect changes in electron temperature. The atomic data were obtained from the CHIANTI (version 5.2) atomic database (e.g., Landi et al. 2006). All lines discussed in this paper are listed in Table 2 with their temperatures of peak formation in ionization equilibrium (Mazzotta et al. 1998).

Since EIS scans from west to east, the western edges of the active regions were observed earlier than the eastern edges. However, all spectral quantities for a given spectral line (e.g., the parameters of a Gaussian fit) compared at any single position in a raster were recorded simultaneously on a single CCD. Therefore, all spectral quantities for a single line

are perfectly co-aligned in position as well as being recorded at the same time.

Observationally we have found that the width of the 195 Å line is slightly larger than the widths of the other Fe XII lines for reasons not yet completely understood. Part of the reason is a blend with another relatively weak Fe XII line. We have quantified the difference by carrying out a detailed comparison between the Fe XII 193.51 Å and 195 Å line widths using data from another active region, from which a width correction factor for the 195 Å line was determined. We have linearly subtracted this correction, 2.605 mÅ, from the 195 Å width in order to derive non-thermal velocities from the 195 Å line. Even without this correction, we also found that we obtain the same qualitative non-thermal line widths with the Fe XIII line at 202 Å as with the 195 Å line, as well as with the Fe XII line near 193 Å. We prefer the stronger 195 Å line rather than the Fe XII 193 Å line for line profile measurements because of its better counting statistics. Subtracting the 2.605 mÅ correction, compared with not subtracting the correction, reduces the Fe XII non-thermal velocity by about 5 km s⁻¹ at around 30 km s⁻¹ and by about 3 km s⁻¹ at about 70 km s⁻¹.

We have reduced the data using the standard EIS software data reduction package. The data were corrected for cosmic ray hits, hot and warm pixels, detector bias, and dark current. Data numbers were converted to intensities in ergs cm⁻² s⁻¹ sr⁻¹ Å⁻¹. An additional effect that was corrected for is a variation of line position over the *Hinode* orbit due to temperature variations in the spectrometer caused mainly by a varying exposure to infrared heating from Earth. This variation produces an approximately sinusoidal variation of spectral line centroids. It is removed by averaging centroid positions over a length of slit for which the underlying solar region is mostly a quiet Sun region without any obvious transient activity. Another correction that was applied is a correction for a slight tilt of the slit on the CCDs, which affects wavelengths along a north/south direction. These corrections allow us to make Doppler maps of active regions in spectral lines for comparisons with the non-thermal velocities, provided rest wavelengths can be determined.

The parameters discussed in this paper are total spectral line intensities, spectral line widths, and spectral line wavelengths. These parameters are determined from the reduced data using a standard Gaussian fitting procedure for each spectral line.

EIS does not have an absolute wavelength calibration source. The wavelength scale for EIS was calibrated as described in Brown et al. (2007). However, in order to make active region Doppler maps, a choice must be made for each active region of a spectral line wavelength that we decide represents zero Doppler velocity. For each active region discussed herein, we have determined this wavelength by averaging low intensity regions over large areas that are outside of the active region. These defined rest wavelengths are within about 0.002 Å or 3 km s⁻¹ of each other.

Previous work with SUMER (e.g., Brekke, Hassler, & Wilhelm 1997; Chae, Yun, & Poland 1998b; Teriaca, Banerjee, & Doyle 1999b) indicates that the average quiet Sun Doppler velocity at the temperature of Fe XII is close to zero, or at most a few kilometers per second. There is some indication that a small velocity for Fe XII would be a blueshift (Teriaca et al. 1999b), which would make the flows we observe slightly larger than we report here. But this needs confirmation.

The non-thermal speed is obtained from the full width at half maximum (FWHM, in mÅ) of the line profile from the expression,

$$FWHM = 1.665 \times 10^3 \frac{\lambda}{c} \sqrt{\frac{2kT}{M} + V^2} \quad , \quad (1)$$

where λ is the wavelength (in Å in this paper), c is the speed of light, k is the Boltzmann constant, T is the electron temperature, and M is the ion mass. Equation (1) assumes that the instrumental width (56 mÅ) has been removed from the line profile and that all broadening mechanisms are Gaussian. Furthermore, if ionization equilibrium is assumed, there is the tacit assumption that the electron and ion temperatures are equal. These assumptions are highly likely valid in the low corona where the EIS observations are made, because electron densities at these altitudes in the corona are on the order of 10^8 to several times 10^9 cm $^{-3}$. At these densities equilibration times between electrons and ions are very short, and ionization and recombination processes are very rapid for ions such as Fe XII.

4. RESULTS

4.1. The August 23, 2007 Active Region

Figure 1 shows a summary of the results for the August 23, 2007 active region. The upper left panel is an intensity plot for the Fe XII 195.12 Å line. The middle and lower left panels show the line centroid shift (colorbar units are mÅ) and FWHM of the line (colorbar units in km s $^{-1}$), respectively. The top right panel shows a co-aligned *Hinode* SOT magnetogram of the area within the boxed region. The middle and bottom right hand panels show the centroid and FWHM respectively within the boxed region shown in the left hand panels.

The striking aspect of Figure 1 is that the Doppler shifts and non-thermal line widths are not only well-correlated, but that the largest values for these quantities occur in regions where the Fe XII line intensity is very low. The Fe X (see Table 2) image does show activity in the area of the flows and non-thermal motions, but it is not spatially correlated well with

the Fe XII features. For the region in Figure 1, the largest Doppler shift speeds (outflows) are on the order of 15-20 km s⁻¹ and the non-thermal speeds become as large as 55-60 km s⁻¹. The SOT magnetogram in Figure 1 indicates that the outflow regions occur over fields of one dominant magnetic polarity, which may indicate either open field lines or long closed loops.

The temperature and density distributions in the flow regions are shown in Figure 2. The upper two panels show the electron temperature and density as a function of the FWHM of the Fe XII line for the region within the box in the upper right panel of Figure 1. The temperature was determined from the Fe XIII to Fe XII line ratio assuming ionization equilibrium and an isothermal plasma. The density was determined from the ratio of the Fe XII lines in Table 2. Figure 1 shows that the FWHM and Doppler shifts are well-correlated, so the data in the upper panels of Figure 2 that correspond to the largest FWHMs also correspond to the largest outflow speeds. There is a clump of data near a FWHM of 70 mÅ and a scattering of points towards larger FWHM that does not either increase or decrease with temperature. These data arise from the outflow regions. The large outflow regions have a characteristic temperature of about 1.2×10^6 K and a density of about 7×10^8 cm⁻³, just above quiet Sun values. Thus the large outflow regions are more representative of quiet Sun regions than active regions.

The bottom two panels of Figure 2 show histograms of the Doppler shift and the FWHM. Both exhibit tails that show the correlation of FWHM with Doppler speed. The data in Figure 2 that clump near 70 mÅ and near zero Doppler speed are from the pixels surrounding the outflow regions. The clear correlation of Doppler speed and non-thermal velocity is shown in Figure 3. These results were obtained by removing the instrumental width from the line profiles and assuming an electron temperature as defined for Figure 2.

The August 23 active region was not bright enough to compare with good statistics the Fe XII outflow speeds and FWHMs with other lines. The strength of the activity was weak enough such that there is no visible sunspot at the location of the active region. However, there is a general positive correlation with similar data from the Fe XIII line in Table 2, and some, but reduced, correlation with the Fe X line. *Transition Region and Coronal Explorer (TRACE)* images show considerable activity in the 171 Å band near the EIS Fe XII outflows, but the spatial correlation of *TRACE* and EIS features is not particularly good.

The spectral line profiles in the wide-line outflow regions look fairly symmetric, with no obvious blueshifted separate component to an otherwise stationary component, as seen in X-ray line profiles at the onset of many flares. This result is similar to that found by Doschek et al. (2007) for an active region observed in December, 2006.

We note that there was considerable activity in the bright part of the August 23 region throughout the time of the EIS raster. Observations with *TRACE* and the Extreme UltraViolet Imagers (EUVI) on the two *Solar Terrestrial Relations Observatory (STEREO)* spacecraft show that the obvious large loop system in the shape of a *u* in the Fe XII intensity image near the center of the image did not exist at the start time of the EIS raster. It is the result of a filament eruption that occurred with the ends of the filament apparently anchored east and west of the outflow regions. The outflow regions do not appear to be involved in any of the activity to the east in the bright part of the active region.

The August 23 region was also observed on August 22, twice during August 23, and once on August 24. The August 22/23 observations cover a 24 hour period and the August 24 observation extends the coverage by about 12 more hours. Outflows in the same general area are seen as in the observation under discussion. Thus the outflows appear to be persistent with lifetimes on the order of at least 1.5 days. This result was also found by Del Zanna (2008), who in addition confirmed the conclusions in Doschek et al. (2007).

4.2. The December 11, 2007 Active Region

Figure 4 shows results for the December 11 active region presented in the same format as in Figure 1. Again, there is a clear separation of the largest outflow regions from the most intense regions in the Fe XII line, and there is a clear correlation between outflows and spectral line widths. And again, the large outflow regions are located in an area of primarily a single polarity. However, the December 11 active region is stronger than the August 23 region and contains a prominent sunspot group.

The SOT G band, Ca H, and magnetogram images of the active region are shown in Figure 5, co-aligned with the EIS FWHM image. It is clear that the large sunspot in the G band image lies south of the large FWHM region. The circular region surrounded by large FWHM regions in the upper left Figure 5 panel is not delineating the sunspot, but rather is close to a region of weak magnetic field, as seen by comparing the magnetogram with the FWHM image. This circular region is also a region of weak Ca H emission. The alignment of the region in the SOT data with the EIS data is not precise, but is within about 2".

Similar results as shown for the August 23 region in Figure 2 are shown for the December 11 region in Figure 6. These results correspond to the data within the boxed area shown in the upper right panel of Figure 4. As found for the August 23 region, pixels for which large FWHM values are derived are characterized by quiet Sun temperatures and relatively low densities. In contrast, the regions immediately surrounding the large width areas

have densities in places that are on the order of 10^{10} cm $^{-3}$ and somewhat higher electron temperatures.

The lower two panels of Figure 6 show histograms of the Doppler shift and FWHM for the Fe XII line. In this case there is clearly a strong outflow component in the Doppler shift histogram, much stronger than for the August 23 region. Although the color scheme in Figure 4 shows where the strongest outflows are coming from, this can be seen more clearly from Figure 7. The upper left panel of Figure 7 shows the Doppler shift, and the black and white images show where Doppler shifts of different magnitudes come from. The white pixels in each image represent those pixels for which the Doppler shift shown in Figure 6 is equal to or less than the value of D_s mÅ specified for each image. Thus the data in the upper right panel of Figure 7 illustrate that all the outflows pixels with Doppler shifts less than -8 mÅ occupy the white area shown. The position of this value of D_s can be seen in the Doppler shift histogram of Figure 6 and it represents essentially all of the outflow regions. The part of the Doppler shift histogram near zero shift in Figure 6 arises from all the regions surrounding the dark region in the upper left panel of Figure 7. As D_s is progressively decreased, the white area is reduced and reveals clearly the regions of strongest Doppler shift. The shift D_s can be converted to a speed V in km s $^{-1}$ by, $V = 3 \times 10^5 \times D_s / 195.120$.

The correlation between non-thermal speed and Doppler shift is given in Figure 8. The non-thermal speeds reach values of about 90 km s $^{-1}$ and the maximum Doppler outflow speeds are on the order of 45 km s $^{-1}$. Note that Doppler shifts as large as 140 km s $^{-1}$, as reported by Sakao et al. (2007) for a different active region, are not observed (However, see Harra et al. 2008).

The December 11 active region is bright enough to examine the outflow images in a number of different spectral lines (see Table 2), formed at different electron temepratures. Results for the December 11 outflow region are shown in Figure 9. In Figure 9 there is a general resemblance of all the outflow images, implying a correlation. However, a close inspection shows that the easternmost (leftmost) outflowing region has approximately the same location in all the images, but the westernmost outflowing region shifts gradually more westward as the temperature of line formation increases. This is clearly seen by comparing the rightmost upper and lower panels in the figure, showing the Fe XII and Fe XV images, respectively. Note also that the fine structure varies among all the images, implying small-scale multi-temperature outflowing regions.

Fe XII line profiles in the outflow regions are symmetric in some areas, particularly the westernmost regions, but in the easternmost regions an asymmetric blue wing appears frequently on profiles. This further supports the concept of multiple flow sites with flows at different Doppler speeds.

Inspection of EIS images for spectral lines other than the Fe XII line formed at lower and higher temperatures, as well as *STEREO/EUVI* movies, shows many long and not too bright loops in the vicinity of the outflows. These loops generally have a westerly component; some are even mostly parallel to the east/west direction. Other loops have substantial southern and northern components.

5. DISCUSSION

From the above analysis of active region dynamics with EIS we may conclude:

1. Extensive areas of active regions where the Fe XII emission line intensity is weak exhibit higher Doppler shift outflows and higher non-thermal velocities than found in other areas of the active regions where the line intensity is much stronger. This does not rule out large flows and line widths in high intensity areas of active regions; we are simply implying that there will be regions of low intensity in active regions that have significant Doppler shift and line width signals. The outflows range from a few km s^{-1} to as much as 50 km s^{-1} . The non-thermal motions range from about 20 to 90 km s^{-1} .
2. The temperatures of the outflow regions obtained from the intensity ratio of an Fe XIII line to an Fe XII line are about $1.4 \times 10^6 \text{ K}$, and electron densities vary from about 5×10^8 to about 10^{10} cm^{-3} , depending on the particular region.
3. The outflow regions are concentrated primarily over or near magnetic regions of a single polarity, and can last for at least periods of a day and a half although there are variations within the flow region.
4. There is some evidence for variations of temperature within flow structures and multiplicity of flows, i.e., the excess widths of the lines need not be due to turbulence even in cases where the line profiles appear well-fit by single Gaussian profiles. It is possible that a wide profile is composed of the line profiles of many outflowing regions, each slightly Doppler shifted with respect to each other due to slightly different Doppler shifts. This scenario might produce a summed wide profile that could be fit with a single Gaussian. A multi-component scenario definitely holds for the 11 December event. Some of the outflow profiles show an obvious secondary outflowing component such that the overall profile departs significantly from a Gaussian.
5. The Fe XII intensity in the outflow regions is much less than in the bright active region loops. However, it is brighter than in a disk coronal hole that was observed by EIS on September 28, 2007 near 01:45 UT. In this coronal hole the Fe XII line is significantly

fainter than in the active region outflow regions.

The faintness of the structures could be due to intermittency in the outflows. That is, if the outflows are events with time scales significantly less than the exposure times, they will appear faint simply because they are bright for only part of the exposure time. For example, two hypothetical regions, equally bright per second, would appear different by a factor of, say, 5 in brightness if one region only lasted 5 seconds while the other lasted for a longer exposure time of 25 seconds. Intermittent events of this nature would have to persist over time intervals of at least a day to explain the persistence of the outflows.

From inspection of context data from a number of spacecraft it appears that the outflow regions are associated with long magnetic flux tubes, and/or open field lines that extend into the heliosphere. It is interesting to calculate the mass flux in the outflowing regions. For the December 11 event the outflow mass flux for all outflows greater than about 12 km s^{-1} in the boxed region of Figure 4 is about $1 \times 10^{-5} \text{ gm cm}^{-2} \text{ s}^{-1}$ and is about $1.6 \times 10^{-6} \text{ g cm}^{-2} \text{ s}^{-1}$ for speeds exceeding 31 km s^{-1} . For the August 23 event the mass outflow flux in the boxed region of Figure 1 is about $5.7 \times 10^{-7} \text{ g cm}^{-2} \text{ s}^{-1}$ for speeds exceeding 12 km s^{-1} . These quantities are obtained by multiplying the flow speed by the mass density for each pixel in the boxed regions with a outflow speed greater than the specified speed, and then summing the result over all pixels.

More investigation is needed to determine whether or not this mass flux, or a fraction of it, contributes to the solar wind. Alternatively, some of the mass flux might be confined within long closed flux tubes. Liewer et al. (2004), Schrijver & DeRosa (2003), Luhmann et al. (2002), Neugebauer et al. (2002), and Wang & Sheeley (2002) have found from data and modeling that active regions can contribute substantially to the heliospheric magnetic field and solar wind. Liewer et al. (2004) find that the open field lines are from the edges of active regions (see Figures 11 and 12 in their paper), in locations similar to where we find the flows discussed in this paper. Schrijver & DeRosa (2003) assert that connections with the heliospheric field to active regions are common, long-lived, and that during solar maximum the contributions of active regions to the interplanetary magnetic field can be as much as 50%. As seen in Liewer et al. (2004), Figure 14 in the Schrijver & DeRosa paper shows open field lines connected to the edge of a plage region. Also, a comparison of their simulation results with the *TRACE* image in their figure shows that the open field regions emanate from a region that is largely dark in the *TRACE* image, qualitatively similar to the locations of the EIS flows in the active regions we have discussed. It is therefore quite tempting to associate at least some of the EIS flows as sources of the solar wind confined to open field lines that extend into the heliosphere.

Some of the Doppler results of this paper are similar to those found by Harra et al.

(2008), who also analyzed flows in an active region discussed previously by Sakao et al. (2007), and these authors suggest that the flows might contribute to the solar wind. These authors found the same types of flows as reported earlier by Doschek et al (2007), but Doschek et al. (2007) did not make a connection with the solar wind.

In addition to the two active regions analyzed in detail in this paper, we have qualitatively examined five other active regions that exhibit similar behavior to the two regions we discussed in detail. However, more studies with EIS will be needed along with simulations of the solar magnetic field in order to test quantitatively the solar wind connection. We are continuing to obtain high resolution rasters of active regions and are refining our knowledge of the zero velocity centroid wavelengths of lines in the EIS spectrum. In particular, deeper exposures that reveal the flows in spectral lines formed over a broad temperature range should be useful in connecting the flows back to their loop footpoint origins. More work also needs to be done on the line profiles in some of the flow regions, which exhibit obvious indications of multiple loop flows.

Hinode is a Japanese mission developed and launched by ISAS/JAXA, collaborating with NAOJ as domestic partner, and NASA (USA) and STFC (UK) as international partners. Scientific operation of the *Hinode* mission is conducted by the *Hinode* science team organized at ISAS/JAXA. This team mainly consists of scientists from institutes in the partner countries. Support for the post-launch operation is provided by JAXA and NAOJ, STFC, NASA, ESA (European Space Agency), and NSC (Norway). We are grateful to the *Hinode* team for all their efforts in the design, build, and operation of the mission.

The authors acknowledge support from the NASA *Hinode* program and from ONR/NRL 6.1 basic research funds.

REFERENCES

Bartoe, J.-D., Advances in Space Research, Vol. 2, No. 4, 185
Boland, B. C. et al. 1975, MNRAS, 171, 697
Brekke, P., Hassler, D. M., & Wilhelm, K. 1997, Sol. Phys., 175, 349
Brown, C. M., Feldman, U., Korendyke, C. M., & Hara, H. 2007, ApJS, in press
Chae, J., Schühle, U., & Lemaire, P. 1998a, ApJ, 505, 957
Chae, J., Yun, H. S., & Poland, A. I. 1998b, ApJS, 114, 151
Cheng, C.-C., Doschek, G. A., & Feldman, U. 1979, ApJ, 227, 1037
Culhane, J. L. et al. 2007, Sol. Phys., 243, 19

Del Zanna, G. 2008, A&A, 481, L49

Doschek, G. A., & Feldman, U. 2000, ApJ, 529, 599

Doschek, G. A., et al. 2007, ApJ, 667, L109

Hansteen, V. 1993, ApJ, 402, 741

Harra, L. K., Sakao, T., Mandrini, C. H., Hara, H., Imada, S., Young, P. R., van Driel-Gesztelyi, L., & Baker, D. 2008, ApJ, 676, L147

Hassler, D. M., Dammasch, I. E., Lemaire, P., Brekke, P., Curdt, W., Mason, H. E., Vial, J.-C., & Wilhelm, K. 1999, Science, 283, 810

Klimchuk, J. A. 2006, Sol. Phys., 234, 41

Korendyke, C. M., et al. 2006, Applied Optics, vol. 45, Issue 34, 8674

Landi, E., Del Zanna, G., Young, P. R., Dere, K. P., Mason, H. E., & Landini, M. 2006, ApJS, 162, 261

Liewer, P. C., Neugebauer, M., & Zurbuchen, T. 2004, Sol. Phys., 223, 209

Luhmann, J. G., Li, Y., Arge, C. N., Gazis, P. R., & Ulrich, R. 2002, J. Geophys. Res., 107, No. A8, 1154

Mariska, J. T., Feldman, U., & Doschek, G. A. 1978, ApJ, 226, 698

Mariska, J. T. 1992, in *The Solar Transition Region*, Cambridge University Press, Cambridge, United Kingdom

Mazzotta, P., Mazzitelli, G., Colafrancesco, S., & Vittorio, N. 1998, A&AS, 133, 403

McIntosh, S. W., Davey, A. R., & Hassler, D. M. 2006, ApJ, 644, L87

McIntosh, S. W., De Pontieu, B., & Tarbell, T. D. 2008, ApJ, 673, L219

Neugebauer, M., Liewer, P. C., Smith, E. J., Skoug, R. M., & Zurbuchen, T. H. 2002, J. Geophys. Res., 107, No. A12, 1488

Parker, E. N. 1988, ApJ, 330, 474

Patsourakos, S., & Klimchuk, J. A. 2006, ApJ, 647, 1452

Sakao, et al. 2007, Science, Vol. 318, 1585

Schrijver, C. J., & DeRosa, M. L. 2003, Sol. Phys., 212, 165

Teriaca, L., Doyle, J. G., Erdelyi, R., Sarro, L. M. 1999a, A&A, 352, L99

Teriaca, L., Banerjee, D., & Doyle, J. G. 1999b, A&A, 349, 636

Tu, C.-Y., Zhou, C., Marsch, E., Xia, L.-D., Zhao, L., Wang, J.-X., & Wilhelm, K. 2005, Science, 308, 519

Wang, Y.-M., & Sheeley, N. R., Jr. 2002, *J. Geophys. Res.*, 107, No. A10, 1302

Warren, H. P., Mariska, J. T., & Wilhelm, K. 1997, *ApJ*, 490, L187

Warren, H. P., & Winebarger, A. R. 2007, *ApJ*, 666, 1245

Table 1: Observed Active Regions in 2007

Date	Time (UT)	Location	EIS Exposure Time (s)
23 August	01 : 55 : 43	$-518'', -211''$	60
11 December	00 : 24 : 16	$-178'', -144''$	60

Table 2: Spectral Lines and Temperatures of Formation

Ion	Wavelength (Å)	Temperature (K)
Fe VIII	185.21	6.3×10^5
Fe X	184.54	1.0×10^6
Fe XII	$186.89 + 186.85$	1.6×10^6
Fe XII	195.12	1.6×10^6
Fe XIII	202.04	1.6×10^6
Fe XIV	274.20	1.8×10^6
Fe XV	284.16	2.0×10^6

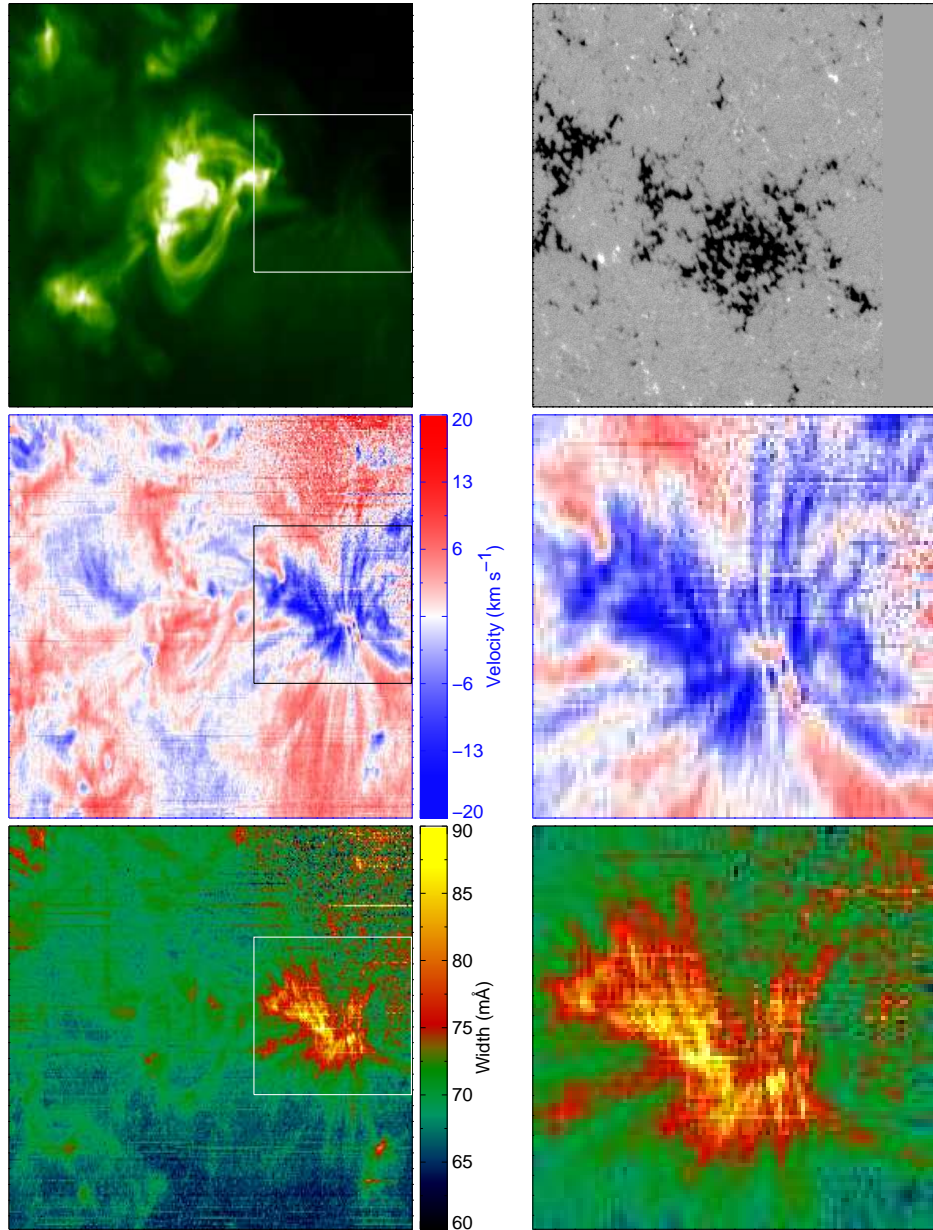


Fig. 1.— Left panels: Top - images of Fe XII 195.12 Å intensity for the August 23 active region; middle - centroid shift (blue is towards the observer); bottom - line width; right panels: top - SOT magnetogram within the boxed region; middle - centroid shift of region in the boxed area in the left panels; bottom - line width within the boxed region. The ordinates are in the north-south direction; the abscissae are in the east-west direction.

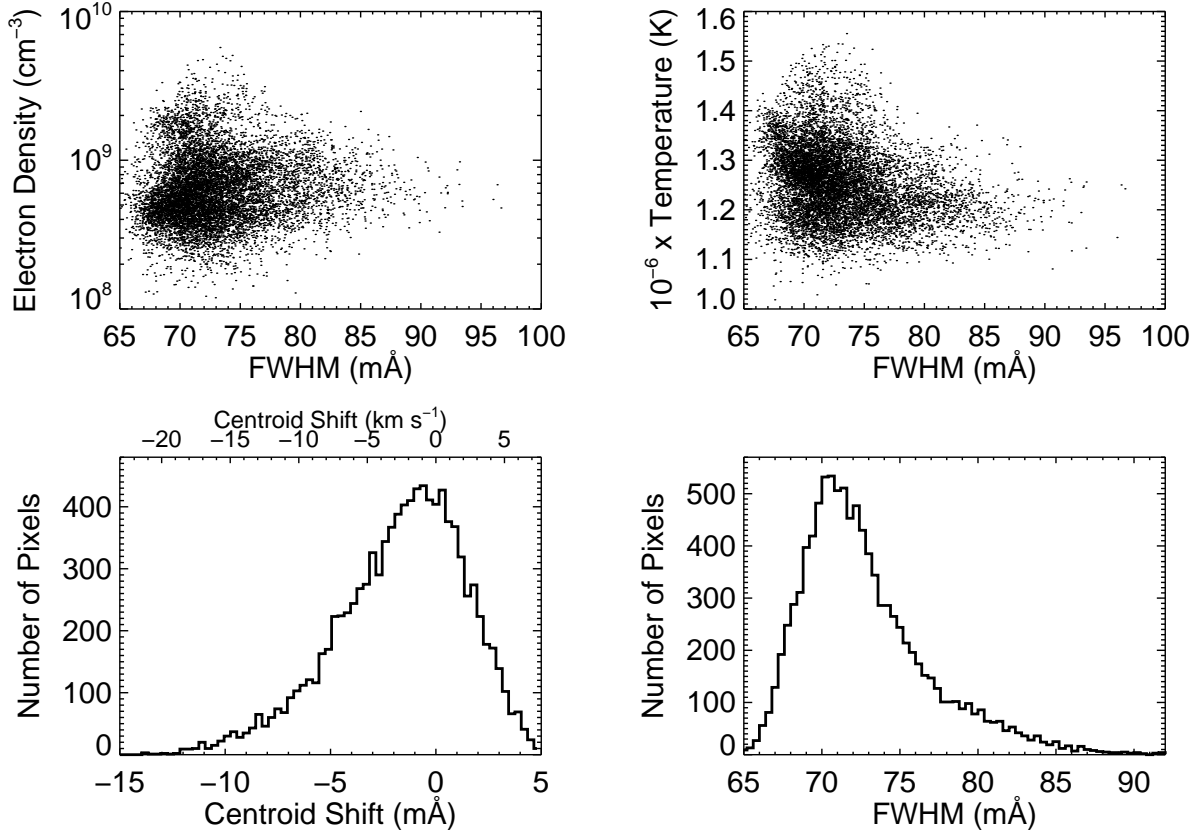


Fig. 2.— Top panels: Electron density and temperature distributions within the boxed area of Figure 1 as a function of FWHM of the Fe XII 195 Å line. The temperature is derived from the Fe XIII/Fe XII ratio. Bottom panels: histograms of centroid shift (left) and FWHM (right) within the boxed area of Figure 1. The centroid shift in $\text{m}\text{\AA}$ is converted to Doppler speed (upper axis). In the bottom right panel, 65 $\text{m}\text{\AA}$ FWHM corresponds to 16 km s^{-1} non-thermal velocity and 92 $\text{m}\text{\AA}$ corresponds to 61 km s^{-1} .

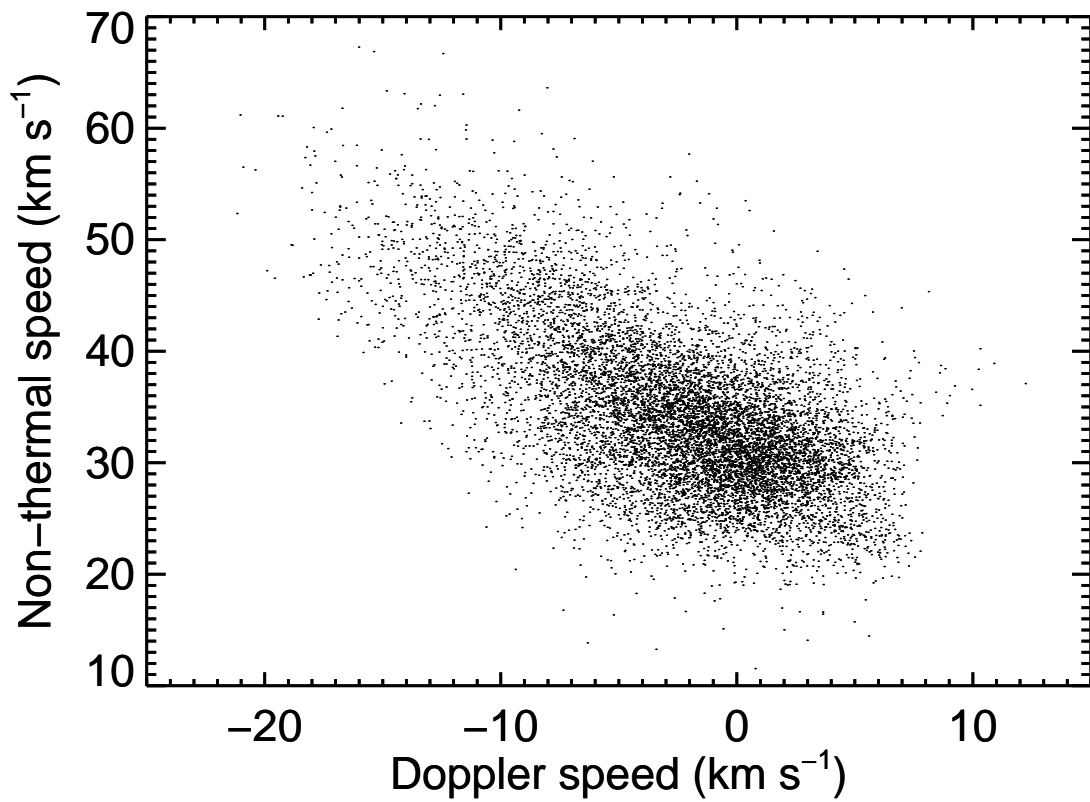


Fig. 3.— Correlation of Doppler speed with non-thermal speed for the data within the boxed area of Figure 1.

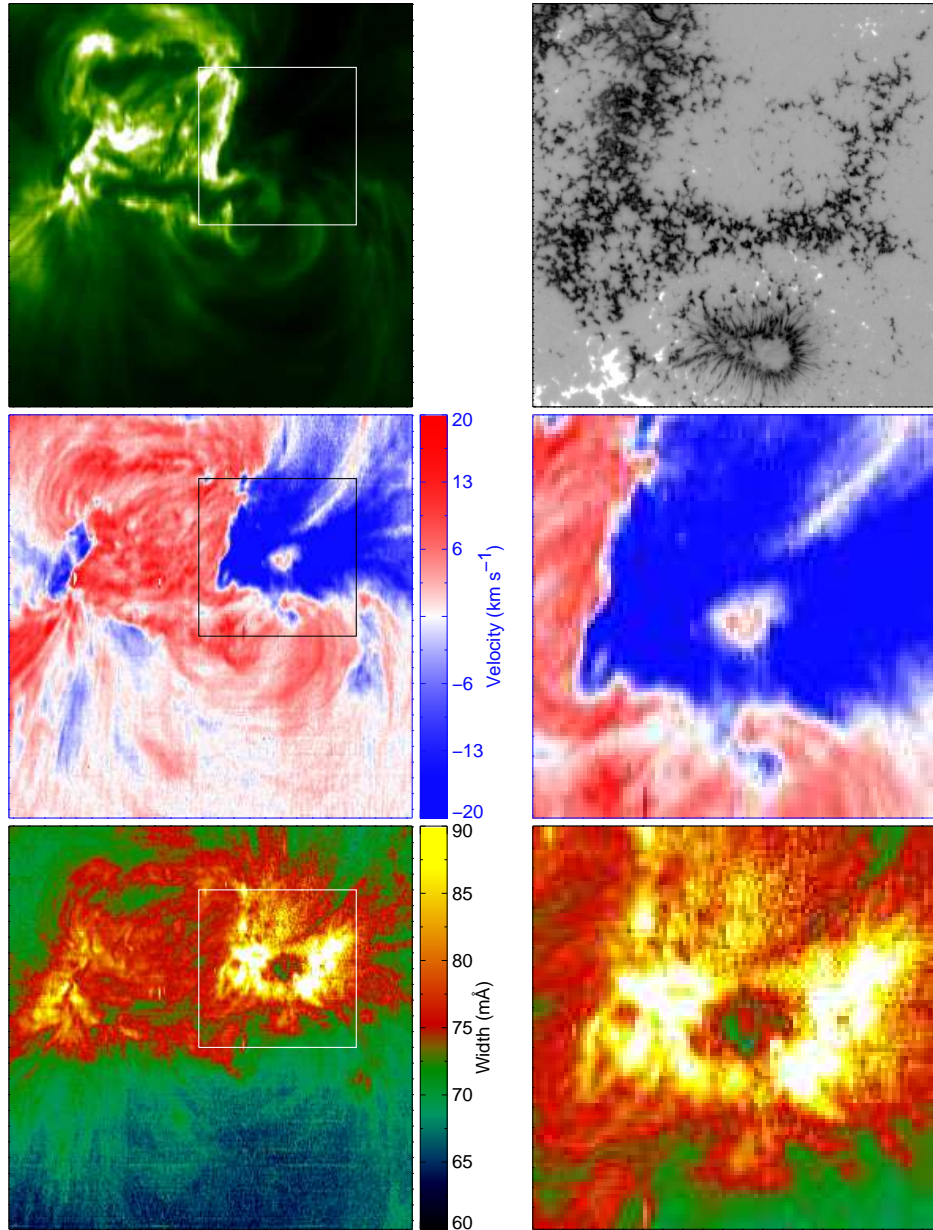


Fig. 4.— Left panels: Top - images of Fe XII 195.12 Å intensity for the December 11 active region; middle - centroid shift (blue is towards the observer); bottom - line width; right panels: top - SOT magnetogram within the boxed region; middle - centroid shift of region in the boxed area in the left panels; bottom - line width within the boxed region. The ordinates are in the north-south direction; the abscissae are in the east-west direction.

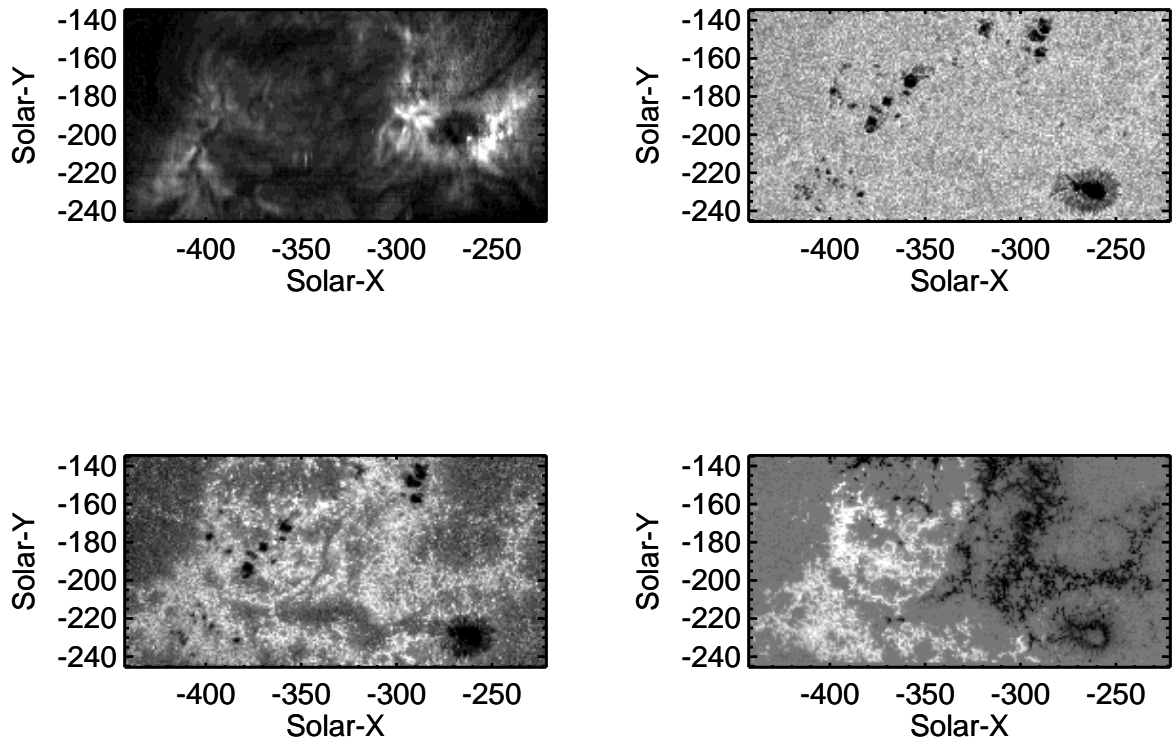


Fig. 5.— Upper left and lower right panels: the Fe XII FWHM and SOT magnetogram shown in Figure 4, respectively. Upper right panel: the SOT G-band image; lower left panel: the SOT Ca H image.

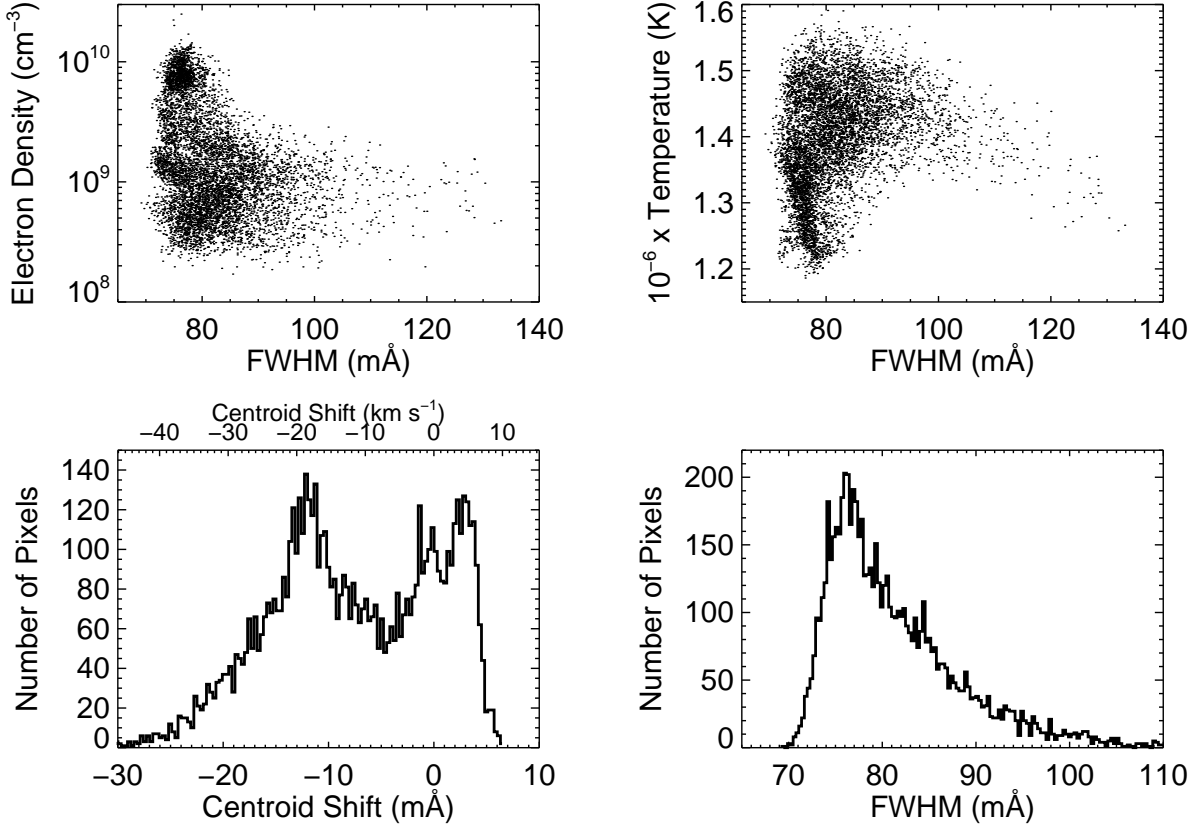


Fig. 6.— Top panels: Electron density and temperature distributions within the boxed area of Figure 4 as a function of FWHM of the Fe XII 195 Å line. The temperature is derived from the Fe XIII/Fe XII ratio. Bottom panels: histograms of centroid shift (left) and FWHM (right) within the boxed area of Figure 4. The centroid shift in $\text{m}\text{\AA}$ is converted to Doppler speed (upper axis). In the bottom right panel, 65 $\text{m}\text{\AA}$ FWHM corresponds to 16 km s^{-1} non-thermal velocity and 110 $\text{m}\text{\AA}$ corresponds to 82 km s^{-1} .

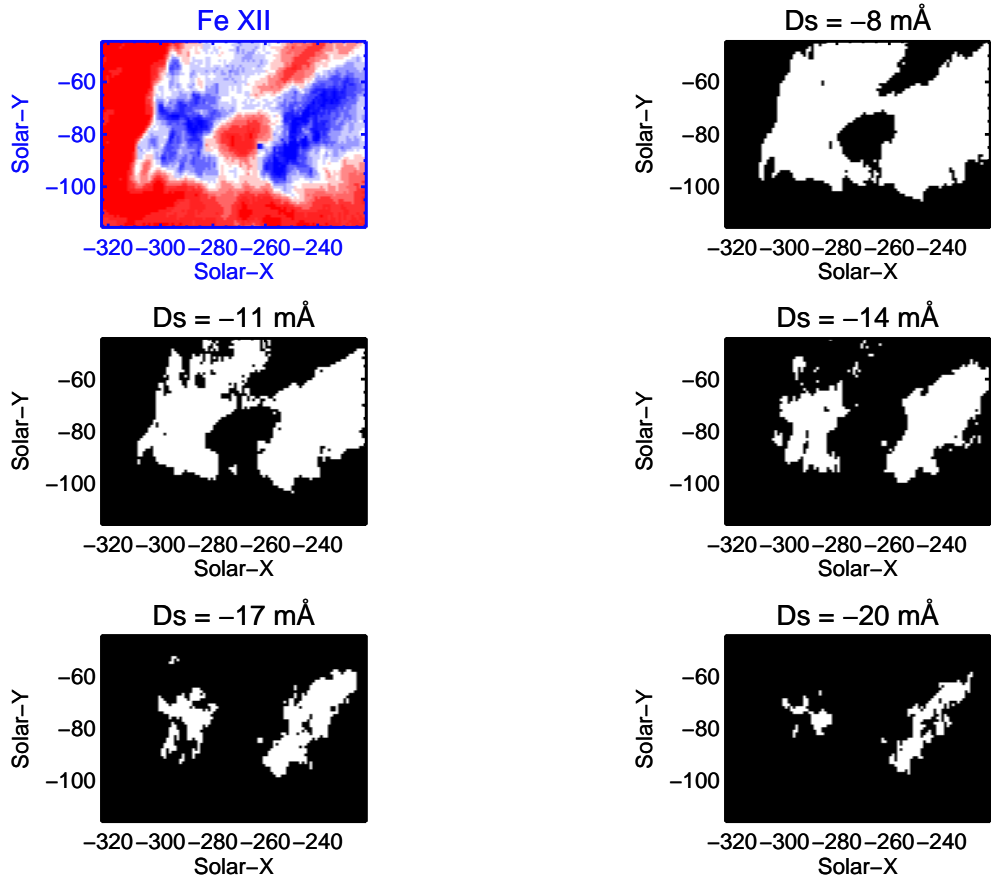


Fig. 7.— Locations of outflows for the December 11 event (see Figure 4) according to magnitude of outflow. The white areas in the black and white figures represent pixels where the Doppler shift is equal to or less than D_s from zero Doppler shift in Angstrom units. Negative D_s is defined as an outflow.

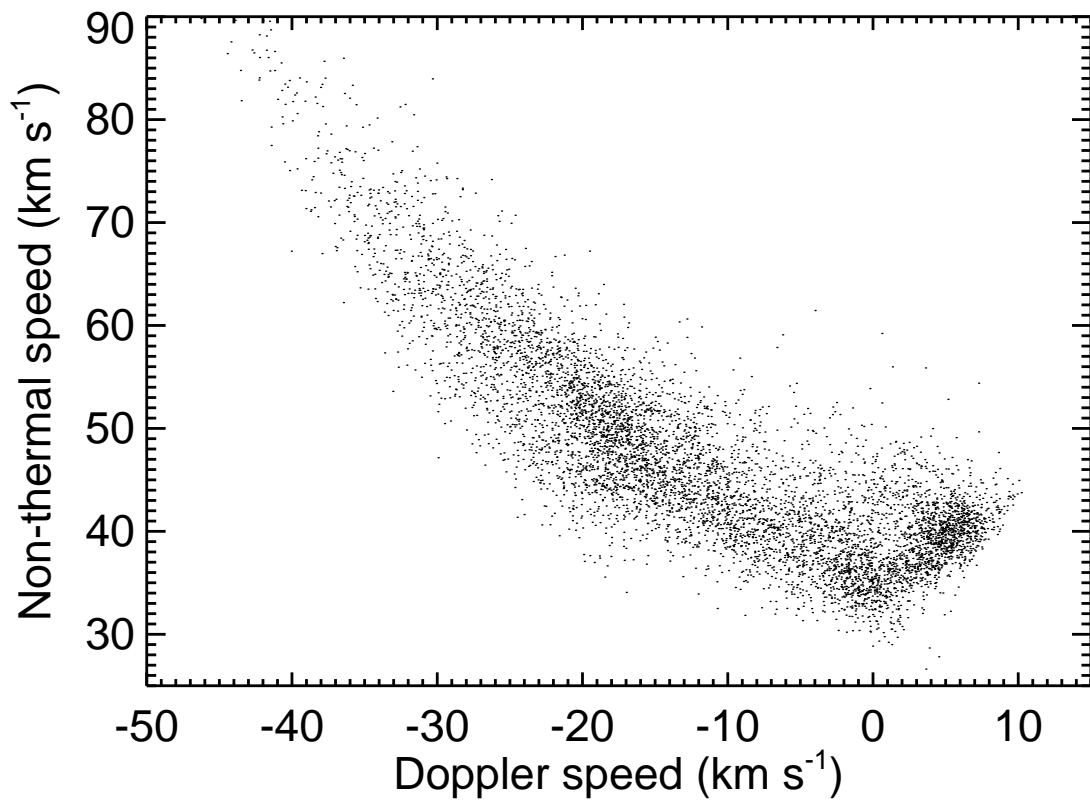


Fig. 8.— Correlation of Doppler speed with non-thermal speed for the data within the boxed area of Figure 4

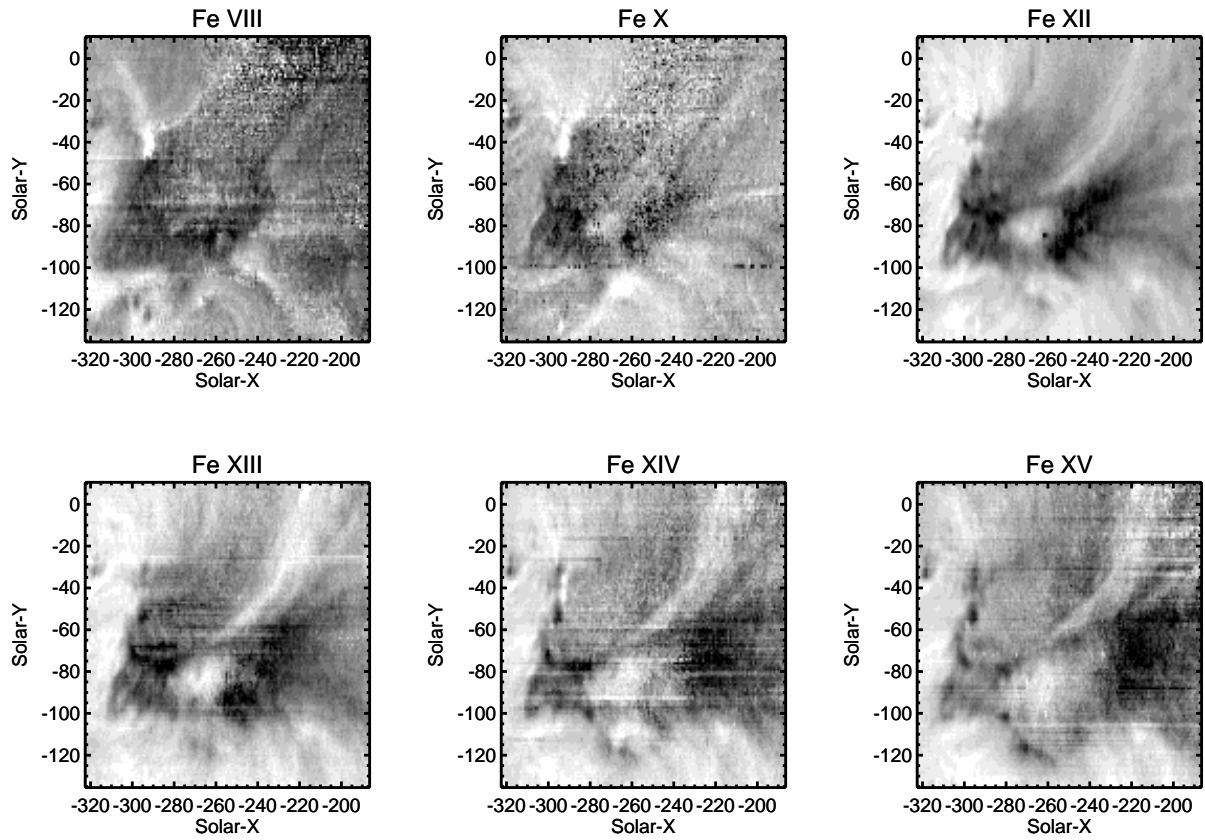


Fig. 9.— Comparison of Doppler shifts interpreted as outflows for the December 11 event (see Figure 4 boxed area) in different spectral lines (see Table 2) formed over a range of temperatures.